A High-Resolution Brillouin Study of GeTe and Carbon-Doped GeTe Nanoscale Films: Implication for Thermoelectric and Memory Applications.

R. Cravero,[†,‡] M. Tomelleri,[¶] J. Paterson,[¶] J. Margueritat,[†] R. Debord,[†] P. Djemia,[§] N. Blanchard,[†] F. Hippert,[‖] O. Bourgeois,[‡] S. Pailhès,[†] P. Noe,[¶] and V. M. Giordano*[,†]

†*Universite Claude Bernard Lyon 1, CNRS, Institut Lumière Matière, UMR5306, F-69100, Villeurbanne, France*

‡*Institut NEEL, CNRS, Université Grenoble Alpes, 25 avenue des Martyrs, F-38042 Grenoble*

¶*Université Grenoble Alpes, CEA, LETI, 38000, Grenoble, France*

§*Laboratoire des Sciences des Procédés et des Matériaux, UPR 3407, Villtaneuse, France*

‖*Université Grenoble Alpes, CNRS, Grenoble INP, LMGP, Grenoble F-38000, France*

E-mail: valentina.giordano@univ-lyon1.fr

Abstract

In this work we report the investigation of the acoustic guided modes in GeTe thin films with different microstructure and nanostructuration, interesting for thermoelectric and memory applications. Specifically, we have studied GeTe thin films where crystallization has been obtained through a controlled annealing up to 400°C and 450°C, which

induces different microstructures, and in a nanocomposite made of nanocrystals of GeTe surrounded by amorphous carbon, recently shown to exhibit a glass-like thermal transport. We have performed a Brillouin scattering investigation on films of three different thicknesses per sample, and on 2 different substrates for one of the samples. This has allowed us to estimate with a good precision the two isotropic elastic constants, and from them the bulk longitudinal and transverse sound velocities for the three samples. We observe that, elastic constants are independent on the annealing temperature and microstructure in GeTe, while, for the nanocomposite, a stiffening is found, in agreement with the estimation of the effective medium elastic moduli following the Reuss approximation. Finally, we have extracted the intrinsic phonon attenuation for the Rayleigh mode, showing a much smaller attenuation in the nanocomposite. This has been interpreted as the consequence of a smaller roughness (finer microstructure, better interfaces) and a smaller anharmonicity in the nanocomposite. This latter finding confirms previous results, and could be possibly related to a modification of the Peierls distortion in GeTe for nanometric grains, calling for further investigations.

Keywords

Germanium Telluride, nanostructure, microstructure, Brillouin spectroscopy, elastic constants, phonons

Introduction

Germanium telluride is a IV-VI compound at the forefront of materials research for its high potential in phase change resistive memories (PCM) in microelectronic devices,[1–3] neuromorphic computing,[4] laser thermal lithography,[5] optically photonic devices[6] as well as for thermoelectric applications.[7–9] Ferroelectric and rhombohedral at room temperature, it has been reported to exhibit a novel kind of atomic bonding, dubbed metavalent, considered to be responsible for a series of properties which make it especially interesting for PCMs and

thermoelectrics.[10,11]

For these reasons, GeTe has been object of a great theoretical and experimental effort in the last decades, aimed at understanding the link between its properties and its atomic structure, stoichiometry and microstructure. If theoretical calculations must face the challenge of correctly reproducing the peculiar inter-atomic interactions in this material, on the experimental side a large variability of properties has been observed, depending on the synthesis procedure. This has been understood in terms of a variable Ge vacancies content with stoichiometry as well as the modifications of the microstructure with the crystallization process.[12,13] As such, many calculated properties lack a definitive experimental verification. This is the case of elastic properties and sound velocity, fundamental bricks of the phonon dynamics and intimately related to thermal transport, for which theoretical studies report a large diversity of values.[14–16]

Despite the relevance of these properties for understanding thermal transport, fundamental in thermoelectric and memory applications, to our knowledge, there is only one indirect measurement of the Debye velocity, as obtained from the experimental phonon density of states,[17] and one estimation of the bulk modulus from diffraction studies at high pressure.[18]

Here we report the experimental measurement of transverse and longitudinal sound velocity in a polycrystalline GeTe thin film annealed at 450°C, as obtained through surface Brillouin Spectroscopy, a no-contact high resolution technique allowing to access the acoustic guided modes in thin films. Moreover, we investigate the dependence of sound velocity and the derivated isotropic elastic constants on the microstructure and nanostructuration, by measuring them also in a GeTe thin film annealed to 400°C and a GeTe-amorphous carbon nanocomposite, whose lattice thermal conductivity has been reported to be glass-like.[19] The comparison of sound attenuation in the three materials allows to identify a strong sensitivity of these acoustic waves to the quality of the interfaces between the thin film and surrounding layers in the stack, and point to a surprising reduced anharmonicity in the nanocomposite.

Experimental section

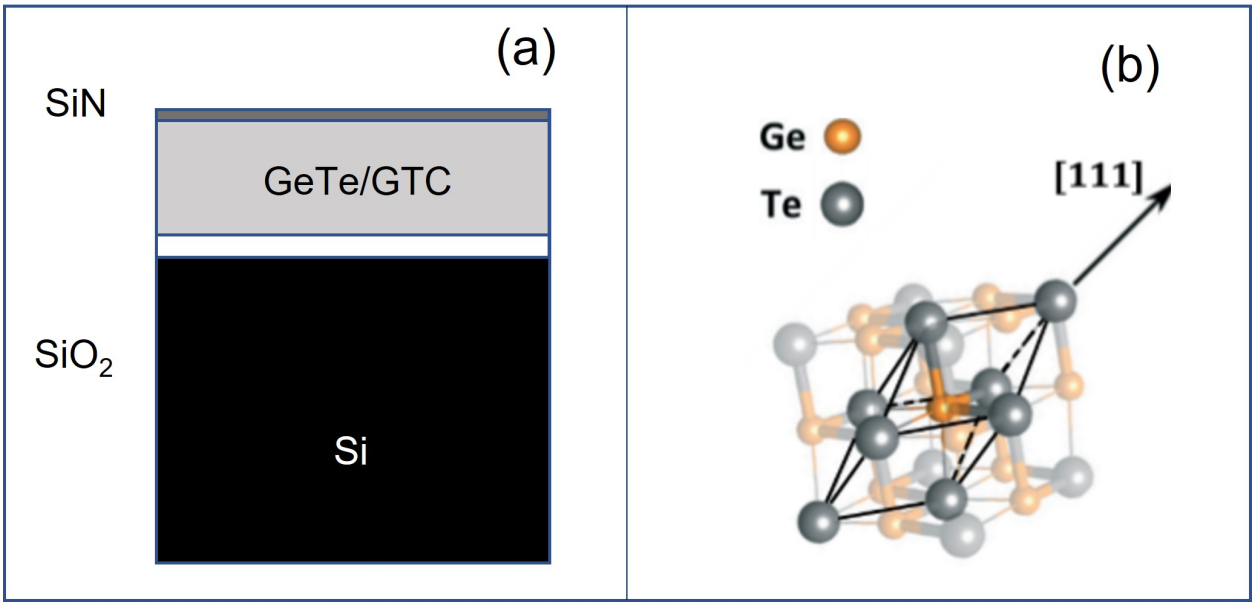

Figure 1: **Sample sketch**. (a): Typical sample stacking. (b): rhombohedral crystalline structure of GeTe, as assessed by x ray diffraction in all samples.

A sketch of our typical samples is reported in Fig. 1 (a). Thin films of variable thickness of the homogeneous amorphous alloy GeTe and $(GeTe)_{1-x}C_x$ with x=0.091 (GTC9) have been synthesized by magnetron co-sputtering from a GeTe and a C target in Argon atmopshere on a 200 nm silicon wafer topped with a 500 nm SiO_2 layer. All the films were then capped *in situ* with amorphous SiN for avoiding any oxidation : PVD SiN was sputtered from a Si target with a 50/50 Ar/N_2 mixture, resulting in a thin film density of 2.9 g/cm^3 and a thickness of 20 nm for GeTe R450 and 10 nm for all other samples. The Ge and Te concentrations were assessed by Rutherford Back Scattering (RBS), while the one of C by Nuclear Reaction Analysis (NRA). The alloys were crystallized during a thermal annealing with a ramp rate of 10 K/min, while monitoring *in situ* the electrical resistivity by a 4 point probe method. The dramatic decrease of the resistivity clearly identifies the crystallization onset and completion.[20,21] GeTe films were crystallized up to 450°C (GeTe R450) and 400°C (GeTe R400), while GTC9 was annealed up to 450°C.[20] During crystallization of GeTe at $\sim 200-230$°C, a significant tensile stress-buildup occurs, however, at the high annealing tem-

peratures here used, the excess Ge, expelled at the crystallization of the rhombohedral GeTe phase, crystallizes, reducing the stress on the crystalline grains and leading to the formation of voids to accomodate it.[22,23] The presence of amorphous carbon at the grain boundaries in GTC9 also contributes to reduce the residual stress, due to its viscous flow.[20,21] In order to establish with better precision the chalcogenide elastic properties, some GeTe R450 samples were also prepared without the SiO_2 layer. For this, GeTe was simultaneously deposited on the two substrates (with and without SiO_2), and crystallization was also performed simultaneously, to get fully comparable samples. We will call the samples on Si GeTe(Si) R450 to distinguish from GeTe R450 on SiO_2.

As reported in our previous work,[19] in all cases GeTe has a rhombohedral structure, exemplified in Fig. 1 (b), with a mass density of 6.24(4) g/cm^3 for pure GeTe and 5.86(4) g/cm^3 for GTC9.[19] All samples were investigated by x ray diffraction at the Henri Longchambon diffraction center in Villeurbanne, using a Bruker D8 diffractometer in a Bragg-Brentano $\theta - 2\theta$ configuration with the copper anode, $\lambda = 1.54$ Å. Samples are all isotropic (random orientation of the crystalline grains) and nanocrystalline, with a typical grain size, as estimated from the x ray diffraction pattern, of 80(10) nm for GeTe R450, 53.6(4) nm for GeTe R400 and $\sim$ 16(3) nm for GTC9. The different annealing temperatures do not affect the intrinsic properties of GeTe, but only the microstructure and thus the quality of the interfaces with the SiN and SiO_2 layers. Diffraction spctra are reported in the Supplementary Information.

Samples were investigated by Scanning Electron Microscopy (SEM), in order to measure their thickness and inspect the microstructure. SEM was conducted using a Tescan CLARA equipped with a high-brightness Schottky emitter. Imaging was performed at a landing energy of 5 keV, using either secondary or backscattered electrons. These electrons were detected by the axial and multidetector electron detectors positioned within the electron column. The thicknesses of the films resulted to be 90(7), 380(10) and 790(10) nm for GeTe R450, 97(7), 380(10) and 990(10) nm for GTC9, while we had only two thicknesses for GeTe

R400, 100(7) and 990(10) nm. Cross-view SEM images are reported for the 800-1000 nm thick films for the three samples in Fig. 2. Voids are present in GeTe R450, due to the crystalline growth, mostly localized at the interfaces. Smaller and fewer voids can be seen in GeTe R400, while GTC9 exhibits a finer and dense microstructure, pointing to a better quality of the interfaces. A summary of grain size and thicknesses of our samples is reported in table 1.

Brillouin scattering experiments were performed in a backscattering configuration. In our setup we used a single longitudinal mode laser (Quantum Torus 660) with wavelength $\lambda = 660$ nm, whose monochromatization was improved via a Fabry-Perot filter. The sample was mounted vertically on a goniometer. A camera objective with focal length 50 mm and f number 5.6 (ratio of the focal length to the objective diameter) was used for focusing the laser beam on the sample and for collecting the light that was back-scattered within its solid angle. The optical path until the sample was assuring a horizontal polarization of the incident beam. Power on the sample was about 100 mW. The scattered light was then sent to a 3-pass Fabry-Perot interferometer by Sandercock for frequency analysis. Spectra were collected in a frequency range of ± 9 GHz (corresponding to a cavity length of 6 mm) and using 256 analyser channels. Entrance and exit pinhole were set to 300 and 450 μm respectively. In the backscattering configuration one can access acoustic waves propagating parallel to the surface, with a momentum $q = \frac{4\pi}{\lambda} sin(\theta)$, with θ the angle between the incident beam and the normal to the surface in the horizontal plane. Our sample being opaque at the probing wavelength, scattering mainly arises from the diffraction of the incident beam on the sample surface, whose height is modified by the guided acoustic waves with a vertical displacement component (ripple-mechanism).[24]

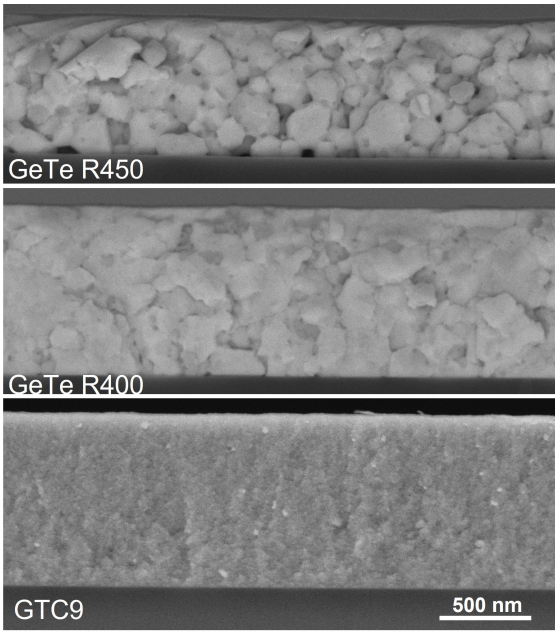

Figure 2: **Microstructure**. The microstructure of the three samples is reported as observed by SEM on the 800-1000 nm thick films. The scale, reported on the bottom right, is the same for all images. A damage on the top left part of GeTe R450 sample is visible, corresponding to a surface bending due to the cleaving of the sample for imaging purposes.

Sample	**GeTe R450**
Grain size (nm)	80 (10)
Film thickness (nm)	90 (7), 380 (10), 790 (10)
Sample	**GeTe R400**
Grain size	53.6 (4)
Film thickness (nm)	100 (7), 990 (10)
Sample	**GTC9**
Grain size	16 (3)
Film thickness (nm)	97 (7), 380 (10), 990 (10)

Table 1: Grain size and investigated film thicknesses for the three kinds of samples.

Results and discussion

Fig. 3 and 4 report our raw data collected on the three samples for thicknesses 100 and ∼1000 nm, at 5 different tilting angles θ from $\sim 30°$ to $\sim 70°$, corresponding to explored wavevectors from 9.5 to 17.9 μm^{-1}. Spectra collected on GeTe R450 and GTC9 films with thickness 380 nm, as well as the spectra collected on GeTe(Si) R450, are reported in the Supplementary Information. Collection time was chosen per sample and scattering angle in order to have a good statistics, spectra were normalized to collection time prior to analysis. From a simple observation, one can see that, in the nanocomposite peaks are narrower and better defined. The single visible peak in the thinner samples in Fig. 3 is the Rayleigh surface mode, which propagates with a sound velocity slightly smaller than the transverse

bulk velocity of the layer. We notice that at the smallest angle, in all samples, this peak appears as a doublet. This is likely due to a contribution to the collected signal from the vertical scattering direction, due to the finite size of the collection angle. In the thicker samples we can clearly see in Fig. 4 higher energy guided modes in GTC9, and in a few cases in GeTe R400 (Sezawa modes). This is not possible in GeTe R450, where the low energy peak is much broader. Fig. 5 reports a direct comparison of spectra collected in the three samples at the two thicknesses, for a scattering angle of 53°, to evidence the emergence of the higher energy modes in the thicker films.

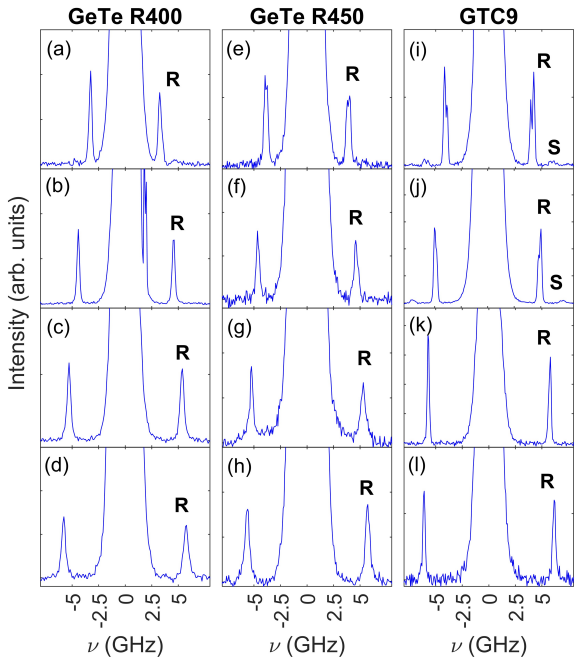

Figure 3: **Experimental spectra**. Brillouin spectra collected on the 100 nm thin films for the three samples. The angle of incidence increases from top to bottom: 26° (a) and 30° (e,i), 40° (b, f, j), 53° (c, g, k) and 63° (d, h, l), corresponding to phonon wavevectors $q = \frac{4\pi}{\lambda} sin(\theta)$ of 8.3, 9.5, 12.2, 15.2 and 17 μm^{-1} respectively. Rayleigh and Sezawa modes are labelled **R** and **S** respectively.

All the spectra have been fitted using a damped harmonic oscillator for the inelastic peaks and a gaussian function for the elastic one. In order to extract the intrinsic phonon width, the theoretical model has been convoluted with the instrumental resolution, as detailed in the Supplementary Information. To estimate the instrumental resolution, we have measured

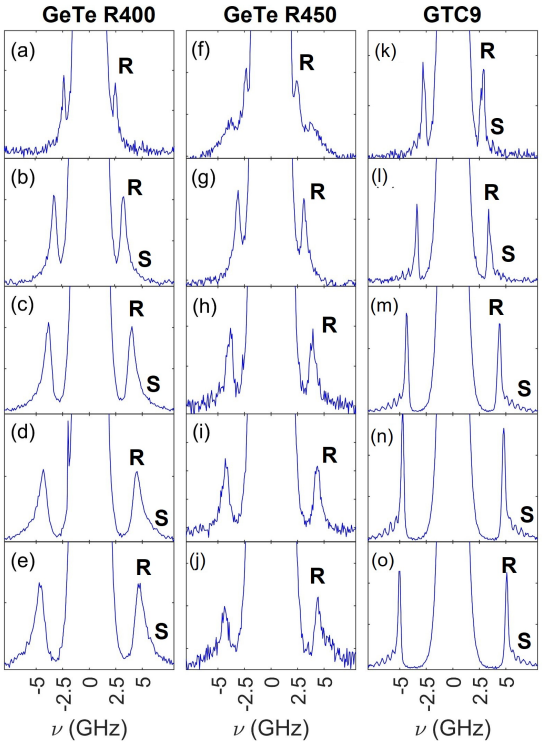

Figure 4: **Experimental spectra**. Brillouin spectra collected on the 800-1000 nm thin films for the three samples. The angle of incidence increases from top to bottom: 30° (a,f,k), 40° (b, g, l), 53° (c, h, m), 63° (d, i, n). and 70° (e, j, o), corresponding to a phonon wavevector of 9.5, 12.2, 15.2, 17 and 17.9 μm^{-1} respectively. Rayleigh and groups of Sezawa modes are labelled **R** and **S** respectively. Note that, for GeTe R400 the Sezawa mode is within the tail of the Rayleigh mode, due to its broadening.

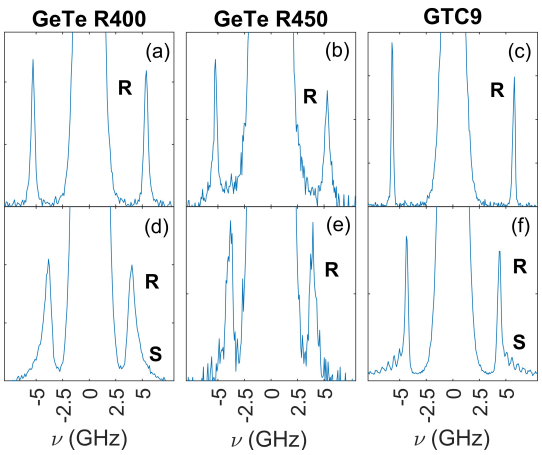

Figure 5: **Emergence of Sezawa modes with thickness**. Brillouin spectra collected on the three samples on the 100 nm (a, b, c) and 800-1000 nm (d, e, f) thin films at a scattering angle of 53°. The larger thickness favours the emergence of the higher order modes (Sezawa modes) in GTC9 and GeTe R400. Note that, for GeTe R400 the Sezawa mode is within the tail of the Rayleigh mode, due to its broadening. Rayleigh and groups of Sezawa modes are labelled **R** and **S** respectively.

the peak corresponding to the elastically scattered light (elastic line) on a copper plate, as well as on the sample itself, at three different angles, to confirm the independence of its width on the probed material and wavevector. The instrumental resolution has been then modelled as a normalized gaussian function with width 0.132(5) GHz, which best fits the elastic line. Some examples of the quality of the fit are reported in the Supplementary Material.

Figure 6 reports the best fitted phonon frequencies for all samples at all probed phonon wavevectors. Both frequency and wavevector are multiplied by the thickness in order to report all films of a given material alltogether. Looking to the GeTe samples, one can see that, in GeTe R400 some Sezawa modes are also visible. Concerning GeTe R450, we have reported in the figure also the results for GeTe(Si) R450. A slight stiffening can be seen for this latter at small qh, corresponding to the 90 nm thick film, which disappears at larger qh. This is indeed the qh region where the guided mode is most sensitive to the different elastic properties of the substrate. Finally, up to 4 guided modes are clearly distinguishable in the nanocomposite. Focusing now on the Rayleigh mode, reported in the bottom panel for the three samples on SiO_2, our data clearly show that GeTe R450 and GeTe R400 share

the same elastic properties, confirming the negligibility of the porosity due to the presence of voids. Concerning the nanocomposite, we can see a slight stiffening.

In order to extract the elastic constants, the equations of motion at the surface of our sample need to be solved taking into account all boundary conditions, that is, all the layers in the stack. We have thus analysed the spectra using a Green function approach of the equations of motion of elasticity, which allows determining the spectral density of the atomic displacements at the free surface, perpendicular to the surface, $u_z(z=0)$. Indeed, the scattered intensity due to the ripple mechanism is proportional to $u_z^2(z=0)$ calculated at a given q.[24,25] As mentioned in the experimental section, all samples are made of crystalline grains randomly oriented, leading to average isotropic properties, despite the intrinsic anisotropy of GeTe rhombohedral phase. In this case, the Green function approach allows determining the relevant isotropic elastic constants (C_{11} and C_{44}), and thus, knowing the density, both longitudinal (v_L) and transverse (v_T) bulk sound velocities.[26] This calculation requires however precise knowledge of all layers in the stack, as the boundary conditions at the sample surface depend on the elastic constants both of the sample and boundary layers. Due to the complexity of the stack of our samples, we have first analysed GeTe(Si) R450. Imposing literature values for the silicon elastic constants and density, we have refined the elastic constants of GeTe R450 and the top layer SiN. Then, we have analysed the GeTe R450 samples with underlying SiO_2 to better refine the GeTe properties and also characterize the SiO_2 elastic constants. Finally, GeTe R400 and GTC9 have been fitted using the already determined properties for the boundary layers. Assuming that the elastic constants do not depend on the sample thickness, the fitting procedure has been repeated on all films of a given sample and all measurement angles, to obtain the best constrained elastic constants. Table 2 reports the refined elastic constants for all layers. As we did not find any notable difference between GeTe R450 and GeTe R400, we report the results grouped for GeTe samples, calling them generically GeTe. First, we notice a fair agreement of our estimated SiO_2 elastic constants with the reported literature values $C_{11}^{SiO_2,lit}$=78.5 GPa and $C_{44}^{SiO_2,lit}$=31.2 GPa.[27] For SiN,the

Young modulus calculated from our estimated elastic constants of SiN and a poisson ratio $\sigma^{SiN} = 0.25$[28] is $E = 2C_{44}^{SiN}(1+\sigma) = 200(100)$ GPa, which compares well with the reported value for PVD SiN at our deposition conditions, $E^{SiN,lit}$=185(5) GPa.[29]

Coming to our samples, the estimated sound velocities are v_T = 1530(100) m/s and v_L = 3500(140) in GeTe, and v_T = 1780(70) m/s and v_L = 3870(50) m/s in GTC9, corresponding to Debye velocities of $v_D(GeTe)$ = 1700(100) m/s and v_D^{GTC9} = 2000(70) m/s. In the literature, there are no other experimental measurements of the elastic constants or sound velocity in GeTe to compare with. Still, the Debye velocity calculated from our results for GeTe is compatible with the one extracted from density of states data, v_D^{DOS} = 1900(70) m/s.[17] Moreover, we obtain a bulk modulus B = 55(6) GPa, well in agreement with the one from x ray diffraction data, B^{XRD} = 49.9(3.2) GPa.[18] Concerning theoretical reports, our estimated elastic constants for GeTe are somewhat smaller than the ones reported in *ab initio* calculations[14–16] for single crystalline material. From these latter, we can calculate the theoretical elastic constants and sound velocities for polycrystalline GeTe following the Voigt and the Reuss approximations, which correspond to uniform strain (Voigt) or stress (Reuss) across the boundaries, and give the upper and lower limits for the real isotropic elastic constants.[30] Using literature data for a GeTe with a density close to ours (6.24 g cm^{-3}[15]), we find that our experimental data are closer to the Reuss estimation. Specifically, the longitudinal velocity is only 5% smaller than the theoretical value, $v_L^{th,Reuss}$ = 3667 m/s. However, the disagreement is larger, of about 30%, for the transverse velocity, for which we calculate $v_T^{th,Reuss}$ = 2166 m/s. This discrepancy could be due to the presence of a large amount of point defects in GeTe, not accounted for in theoretical calculations, pointing thus to a major effect of defects on the shear elastic constant. Concerning the nanocomposite, the observed stiffening can be expected, due to the presence of amorphous carbon, which has a higher sound velocity. Using the measured elastic constants for GeTe, and values from literature for amorphous carbon, we can estimate the expected effective medium elastic constants for GTC9. As reported elsewhere,[19] the density of our amorphous

carbon has been estimated to be 2 g/cm^3, and its volume content in GTC9 only 3%. Using the young modulus and poisson ratio reported for our carbon density in the literature,[31] we find C_{11}^{a-C}=360(20) GPa and C_{44}^{a-C}=147(9) GPa for amorphous carbon. We can now calculate the composite elastic constants and we obtain C_{11}^{Voigt}=83(6) GPa and C_{44}^{Voigt}=18(2) GPa using the Voigt approximation, and C_{11}^{Reuss}=76(7) GPa and C_{44}^{Reuss}=14(2) GPa using the Reuss approximation. Here again, our data are closer to the Reuss values.

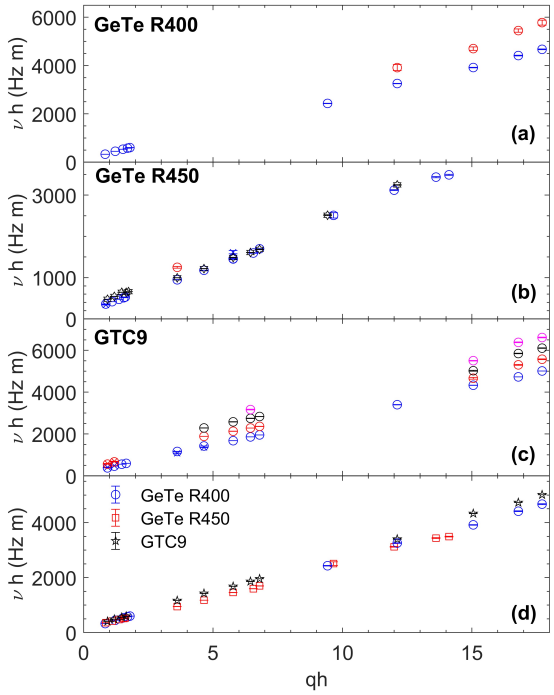

Figure 6: **Experimental dispersions**. The best fitted frequencies are reported multiplied by the film thickness as a function of the wavevector multiplied by the film thickness for the three samples : GeTe R400 (a), GeTe R450 (b) and GTC9 (c). In (a), (b) and (c) the Rayleigh mode is reported as blue circles, higher frequency modes as circles with different color : red for the second mode, black the third, magenta the fourth. In (b) we report as well the Rayleigh mode as measured on GeTe(Si) R450 as black hexagones. Panel (d) reports only the experimental points belonging to the Rayleigh mode for all samples on SiO_2: GeTe R400 (blue circles), GeTe R450 (red squares) and GTC9 (black stars), showing a slight stiffening in the nanocomposite.

We look now to the attenuation of the Rayleigh wave, reported in Fig. 7 for all the investigated stackings. From the figure it is clearly visible that, phonon width in GTC9 is much smaller than in the GeTe samples at all phonon energies. As for GeTe, we observe that

Table 2: Elastic constants as determined by Brillouin light scattering in GeTe and GTC9 thin films, as well as in the boundary layers. In GeTe and GTC9 we have imposed the isotropy condition $C_{12} = C_{11} - 2C_{44}$.

	GeTe	GTC9	Si	SiO_2	SiN
C_{11} (GPa)	74(6)	78(3)	166	77(7)	190(70)
C_{44} (GPa)	14(2)	16(2)	79.6	31(5)	82(50)
C_{12} (GPa)	46(10)	45(6)	64	15(10)	25(10)

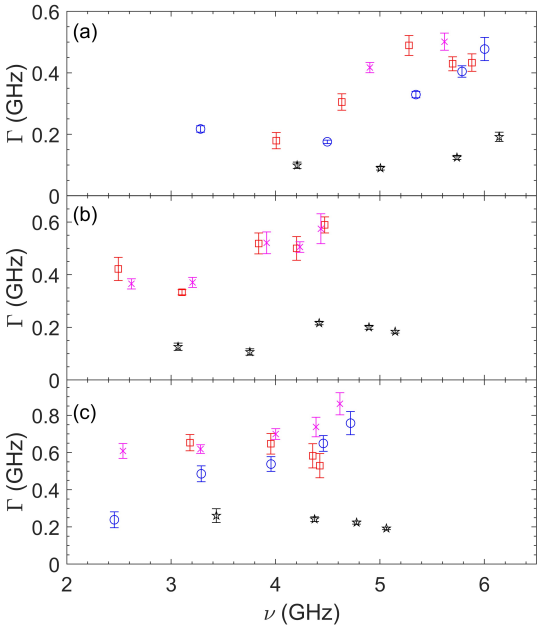

Figure 7: **Experimental attenuation of the Rayleigh wave**. The best fitted phonon widths for the Rayleigh mode are reported as a function of phonon frequency for the $\sim$ 100 nm (a), $\sim$ 380 nm (b) and 800-1000 nm (c) thick films for GeTe R400 (blue circles), GeTe R450 (red squares), GeTe(Si) R450 (magenta x) and GTC9 (black stars).

phonon width is independent on the substrate in GeTe R450, while it seems slightly smaller in GeTe R400. In order to go further and analyse phonon attenuation in terms of scattering processes, we need to extract the intrinsic phonon width. Indeed, the reported width has still a contribution coming from the wavevector instrumental resolution. Due to the finite size of the collection angle, the experimental signal is in fact the superposition of phonons with a range of scattering wavevectors both in the scattering plane and perpendicular to it. In the scattering plane, the probed wavevector will range from $q_L = \frac{2\pi}{\lambda}(sin(\theta) + sin(\theta - \delta))$ to $q_H = \frac{2\pi}{\lambda}(sin(\theta) + sin(\theta + \delta))$, with δ the half angle of the collecting optics. As the mode

is dispersive, for each q in such wavevector range Δq, the energy will be different. As a consequence, an instrumental energy broadening appears $\Delta\nu_{\Delta q} = v_g \Delta q$ with v_g the group velocity at the probed q values. Due to the entrance lens in the spectrometer, in our setup it is $\delta = 1.6°$. Using this datum and our measured dispersions, we have estimated $\Delta\nu_{\Delta q}$ and subtracted it from the measured width to obtain the intrinsic width: $\Gamma_i = \sqrt{\Gamma^2 - (\Delta\nu_{\Delta q})^2}$. This latter is reported in Fig. 8: the values are only slightly smaller and the global behavior is the same as in Fig. 7.

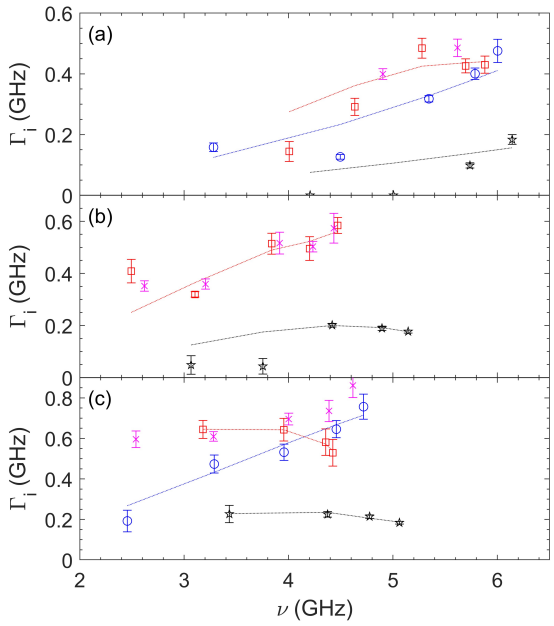

Figure 8: **Intrinsic attenuation of the Rayleigh wave**. The extracted intrinsic phonon widths for the Rayleigh mode are reported as a function of phonon frequency for the $\sim$ 100 nm (a), $\sim$ 380 nm (b) and 800-1000 nm (c) thick films for GeTe R400 (blue circles), GeTe R450 (red squares), GeTe(Si) R450 (magenta x) and GTC9 (black stars). Dotted lines represent the best fit using two scattering mechanisms, the anharmonic scattering and scattering from boundaries, as explained in the text.

First of all, it is worth noticing that, the Rayleigh wave is a surface wave. As such, its properties are essentially sensitive to the upper part of the sample and the top interface. We thus don't expect any contribution to phonon attenuation coming from a possible perpendicular density gradient due to the possible persistence of a crystallization-induced residual stress. We have then analysed the intrinsic attenuation owing for two scattering mecha-

nisms: anharmonic scattering and scattering from the boundaries, which are expected to be the only relevant mechanisms at these wavelengths, as defect scattering is usually dominant at wavelengths in the sub-nanometer range. We have nevertheless verified the negligibility of this contribution to attenuation, by calculating it using a simple analytical model successfully used in mass disorder alloys:[32,33] this gives $\Gamma_{\text{def}} = \pi/2(\hbar\omega)^2 g(\hbar\omega)\langle\epsilon^2\rangle$, where $g(\hbar\omega)$ is the phonon density of states (DOS), and ϵ represents the sum of all fluctuations contributions (mass, elastic constants, atomic size).[34] In our previous work,[19] we have reported our experimentally measured DOS, however data are limited to energies above 0.5 THz.[19] . We use thus the Debye model, with our estimated Debye velocities, for describing the low energy DOS, which was shown to be reached already in the sub-THz range.[19] Concerning the fluctuation term, it may be exactly calculated once the defect density is known. This corresponds to half the carrier density, which has been previously measured,[19] and reported to be $n = 2.7(1) \cdot 10^{20}$ cm^{-3} in GeTe and $n = 11.1(1) \cdot 10^{20}$ cm^{-3} in GTC9. As shown in the Supplementary Information, we find that the defect scattering contribution does increase in the nanocomposite, as expected due to the larger defect density, but remains in the Hz range at the investigated phonon energies, thus fully negligible on our scale.

Concerning the other two contributions, we model the anharmonic attenuation following Slack,[35] $\Gamma_U(\nu, T) = AT(2\pi\nu)^2 e^{(-\frac{\Theta_D}{3T})}$, where A contains material-specific parameters and $\Theta_D = 180$ K is the Debye temperature of GeTe.[36] As for the boundary scattering, we model it using the formulation by Ziman,[37] modulated by a transmission coefficient,[38] which depends on the acoustic impedence mismatch between our sample and the adjacent layers (SiO_2 and SiN) : $\Gamma_b = \frac{1-p}{1+p}\frac{v_g}{d}T_R$, with $p = e^{-16\pi^2\eta^2/\lambda_{ph}^2}$ the specularity parameter, η the roughness at the interfaces, d the film thickness, T_R the transmission coefficient, λ_{ph} the phonon wavelength and v_g its group velocity. Using the experimentally reported mass densities, and the previously calculated Debye velocities, we estimate the acoustic impedence of GeTe as $Z_{GeTe} = \rho_M v_D = 108(7)10^5$ Kg m^{-2}s^{-1} and for the nanocomposite $Z_{GTC9} = 117(5)10^5$ Kg m^{-2}s^{-1}. As the adjacent layers are the same, this means that the transmission won't change

significantly between the different samples. In order to minimize the number of free parameters, due to the few experimental points, we decide thus to fix T_R to the same value for all samples and only fit the anharmonic parameter A and the roughness η. Here we report results for T_R=0.5, while in the Supplementary Information, we report results for a fixed value $T_R = 1$, showing that the difference is very small and plays only on the absolute value of η, while the tendencies remain the same. Finally, it is worth mentioning that, we have also verified that scattering from grain boundaries due to the nanocrystalline nature of the films is negligible at the probed phonon wavelengths. Following the Mathiessen rule for independent scattering mechanisms, the total attenuation will be $\Gamma = \Gamma_U + \Gamma_b$. We have then fitted our data, per sample and per thickness, using this model, as reported in Fig. 8. The best fit values for A and η are reported as a function of thickness for GeTe R400, GeTe R450 and GTC9 in Fig. 9 and in table 3. Independently on the absolute value of the roughness, which is uncertain due to its dependence on the choice of T_R, we can notice that, in all samples the roughness increases linearly with the film thickness. While GeTe R400 and GTC9 present a comparable roughness, the absolute roughness in GeTe R450 is larger and increases faster with thickness, likely due to the accumulation of voids at the boundaries. Concerning anharmonicity, GeTe R450 and GeTe R400 present similar values, which are comparable to but larger than the theoretical anharmonic parameter reported in the literature ($A \sim 110$ ns/K[39]). In that case, the GeTe model had five times less carrier concentration than our samples. This could locally deform the crystalline structure, due to defects, and thus affect anharmonicity. Interestingly, the anharmonic parameter is much smaller in GTC9, in agreement with the suggested lower anharmonicity found in our recent investigation of THz phonon dynamics and thermal conductivity in this material.[19]

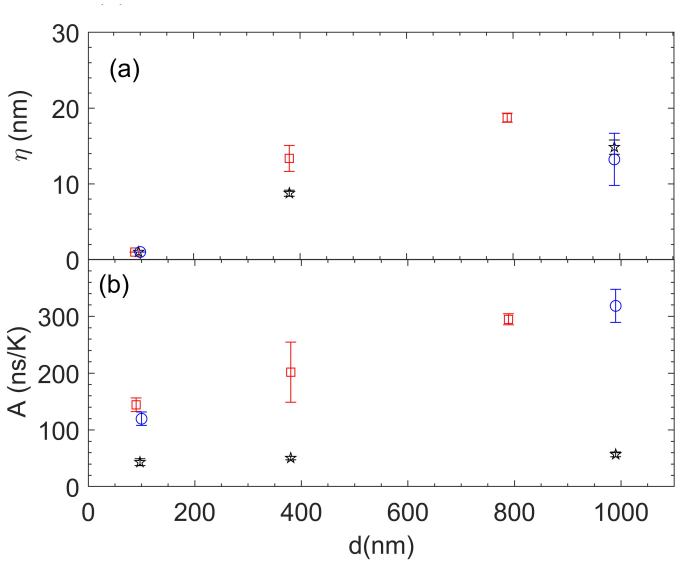

Figure 9: **Fitting parameters for attenuation**. Roughness η (panel (a)) and anharmonic parameter A (panel (b)) are reported as a function of film thickness for GeTe R400 (blue circles), GeTe R450 (red squares) and GTC9 (black stars), for the choice $T_R = 0.5$ (see main text).

Table 3: Fitting parameters for phonon attenuation in all samples. In films with thickness ~ 100 nm, the fit was giving a vanishing roughness, no physical, so we imposed a minimum value of 1 nm. As a consequence, there is no error associated to it in the table.

Sample	thickness	A (ns/K)	η (nm)
GeTe R450	90(7)	140(10)	1
	380(10)	200(50)	19(2)
	790(10)	294(9)	26.5(8)
GeTe R400	100(7)	120(10)	1
	990(10)	320(30)	19(5)
GTC9	97(7)	43(6)	1
	380(10)	50(3)	12.4(6)
	990(10)	57(4)	21(1)

Conclusions

In this work, we have presented a Brillouin scattering investigation of GeTe-based materials interesting for thermoelectric and memory applications. Specifically, we have studied thin films of GeTe at two different annealing temperatures and a nanocomposite made of nanograins of GeTe surrounded by amorphous carbon, GTC9. Our measurements, performed in a backscattering geometry, have allowed us to access the guided modes propagating along

the thin films, and specifically the Rayleigh mode and, in some cases, the Sezawa modes. Data have been collected on different thicknesses per sample, and, in the case of GeTe annealed to 450°C, on two different substrates. By fitting all our spectra using a Green function approach, we have been able to constraint the isotropic elastic constants C_{11}, C_{12}, C_{44}, and determine the bulk longitudinal and transverse velocities. This represents the first direct measurement of such quantities in GeTe films. We have shown that our results on GeTe are independent on the annealing temperature and are smaller than reported theoretical values, pointing to an effect of defects on the elastic properties, and specifically on the shear constant. This should motivate new *ab initio* calculations investigating the relation between defects and elastic properties in GeTe. Moreover, we have shown that the nanocomposite presents a slight stiffening of its elastic constants, which is in good agreement with the Reuss estimation of the effective elastic moduli in a composite material. Next, we have focused on the phonon attenuation for the Rayleigh mode, to get insight onto the relevant scattering mechanisms and their dependence on microstructure and nanostructuration. By fitting our data with a damped oscillator model convoluted with the instrumental energy resolution, and accounting for the additional energy broadening due to the finite size of the collection angle, we could extract the intrinsic phonon attenuation. We have modelled it using two scattering mechanisms, anharmonicity and boundary scattering, and we have shown that while anharmonicity does not depend on the annealing temperature in GeTe, boundary scattering is instead larger in GeTe R450, owing to the presence of voids at the interfaces in this latter. Concerning the nanocomposite, the estimated roughness is comparable to GeTe R400, as expected due to its fine microstructure and nice interfaces. Suprisingly, we find in GTC9 a much smaller anharmonicity. This is in agreement with a recent work of us on THz phonon dynamics,[19] where our results pointed to a reduced anharmonicity. Specifically, our measurements of the density of states revealed a much smaller anharmonicity-driven softening of the optic modes with temperature, and the anharmonic contribution to phonon scattering was found to be negligible in the fit of the thermal conductivity as a function of

temperature. This result is surprising as GTC9 is in principle made of the same crystalline material as GeTe. In fact, as we have previously shown,[19] in the nanocomposite GeTe grains are much smaller and their vacancy content is much larger than in pure GeTe films. Lower anharmonicity could then be related to these two major differences with GeTe. Specifically, the smaller grain size could induce a modification of the Peierls distortion, which can not be evaluated from x ray diffraction due to the broadening of the Bragg peaks. Moreover, a larger vacancy content means larger strain within the crystalline structure. Both effects would affect the metavalent bonding reported for this material[10] and crystal anharmonicity. Further investigations are necessary to shed light on the microscopic origin of the observed reduction of anharmonicity in the nanocomposite.

Credit authorship contribution statement

V.M.G. and P.N. conceived and directed the project. V.M.G. conceived the phonon dynamics investigation, performed some of the experiments, supervised the experimental data analysis and interpretation. R. Cravero performed the experiments and analysis. M. Tomelleri and J. Paterson synthesized and characterized the samples in LETI clean rooms under the supervision of P.N.. J. Margueritat gave technical support on the spectrometer and participated to the scientific discussions. R. Debord gave support during the experiments. P. Djemia is the author of the fitting program based on the Green funciton approach and supervisioned the analysis. N. Blanchard performed the SEM investigation. O. Bourgeois, F. Hippert and S. Pailhès participated to the discussions and interpretation. V.M.G. wrote the manuscript, the co-authors participated to the revisions.

Declaration of competing interest

The authors declare no competing interests.

Data Availability

Data are available on the Zenodo platform with DOI: 10.5281/zenodo.15016898

Acknowledgement

This work was supported by the ANR (project MAPS-ANR-20-CE05-0046 2019) and from the AURA region (Pack Ambition Recherche, project NanoCharme 2018). SEM measurements were performed at PNNL@ILMTech.

Supporting Information Available

Supporting Information: x ray diffraction characterization, additional Brillouin spectra collected on the 380 nm thick films, and on GeTe(Si) R450, an example of fit, with the detailed fitting function for Brillouin spectra, estimation of the attenuation contribution due to defects scattering, fitted roughness and anharmonicity for a different transmission at boundaries.

References

(1) Hamann, H. F.; O'Boyle, M.; Martin, Y. C.; Rooks, M.; Wickramasinghe, H. K. Ultra-high-density phase-change storage and memory. *Nat. Mater.* **2006**, *5*, 383–387.

(2) Noé, P.; Vallée, C.; Hippert, F.; Fillot, F.; Raty, J.-Y. Phase-change materials for non-volatile memory devices: from technological challenges to materials science issues. *Semicond. Sci. Technol.* **2017**, *33*, 013002.

(3) Redaelli, A., Ed. *Phase Change Memory*; Springer International Publishing, 2018.

(4) P. Noé, e. M. W., B. J. Kooi Phase-Change and Ovonic Materials (fifth edition). *Phys. Status Solidi - Rapid Res. Lett.*. **2024**, *18*, 2400239.

(5) Wei, J.; Zhang, K.; Wei, T.; Wang, Y.; Wu, Y.; Xiao, M. High-speed maskless nanolithography with visible light based on photothermal localization. *Sci. Rep.* **2017**, *7*, 43892.

(6) Pavanello, F.; Charbonnier, B.; Noe, P. Phase-change materials for photonic applications. *Photoniques* **2024**, *125*, 45–49.

(7) Li, J.; Zhang, X.; Wang, X.; Bu, Z.; Zheng, L.; Zhou, B.; Xiong, F.; Chen, Y.; Pei, Y. High-Performance GeTe Thermoelectrics in Both Rhombohedral and Cubic Phases. *J. Am. Chem. Soc.* **2018**, *140*, 16190–16197.

(8) Hong, M.; Zou, J.; Chen, Z.-G. Thermoelectric GeTe with Diverse Degrees of Freedom Having Secured Superhigh Performance. *Adv. Mater.* **2019**, *31*, 1807071.

(9) Hong, M.; Li, M.; Wang, Y.; Shi, X.-L.; Chen, Z.-G. Advances in Versatile GeTe Thermoelectrics from Materials to Devices. *Adv. Mater.* **2022**, *35*, 2208272.

(10) Yu, Y.; Cagnoni, M.; Cojocaru-Mirédin, O.; Wuttig, M. Chalcogenide Thermoelectrics Empowered by an Unconventional Bonding Mechanism. *Adv. Funct. Mater.* **2020**, *30*, 1904862.

(11) Raty, J.-Y.; Wuttig, M. The interplay between Peierls distortions and metavalent bonding in IV–VI compounds: comparing GeTe with related monochalcogenides. *J. Phys. D: Appl. Phys.* **2020**, *53*, 234002.

(12) Dong, J.; Sun, F.-H.; Tang, H.; Pei, J.; Zhuang, H.-L.; Hu, H.-H.; Zhang, B.-P.; Pan, Y.; Li, J.-F. Medium-temperature thermoelectric GeTe: vacancy suppression and band structure engineering leading to high performance. *Energy Environ Sci.* **2019**, *12*, 1396.

(13) Li, M.; Shi, X.; Chen, Z. Trends in GeTe Thermoelectrics: From Fundamentals to Applications. *Adv. Funct. Mater.* **2024**, *34*, 2403498.

(14) Singh, J.; Singh, G.; Tripathi, S. Electronic and elastic properties of rhombohedral GeTe: Exfoliation energy of a monolayer from (111) surface. *Mater. Today* **2020**, *28*, 1771–1775.

(15) Shaltaf, R.; Durgun, E.; Raty, J.-Y.; Ghosez, P.; Gonze, X. Dynamical, dielectric, and elastic properties of GeTe investigated with first-principles density functional theory. *Phys. Rev. B* **2008**, *78*, 205203.

(16) Kagdada, H. L.; Jha, P. K.; Śpiewak, P.; Kurzydłowski, K. J. Structural stability, dynamical stability, thermoelectric properties, and elastic properties of GeTe at high pressure. *Phys. Rev. B* **2018**, *97*, 134105.

(17) Pereira, P. B.; Sergueev, I.; Gorsse, S.; Dadda, J.; Müller, E.; Hermann, R. P. Lattice dynamics and structure of GeTe, SnTe and PbTe. *Phys. Status Solidi (b)* **2013**, *250*, 1300–1307.

(18) Onodera, A.; Sakamoto, I.; Fujii, Y.; Mori, N.; Sugai, S. Structural and electrical properties of GeSe and GeTe at high pressure. *Phys. Rev. B* **1997**, *56*, 7935–7941.

(19) Cravero, R.; Tlili, A.; Paterson, J.; Tomelleri, M.; Marcello, P.; Debord, R.; Pailhès, S.; Bourgeois, O.; Hippert, F.; Le Qui, D.; Raty, J.; Noe, P.; Giordano, V. M. Glass-Like Phonon Dynamics and Thermal Transport in a GeTe Nano-Composite at Low Temperature. *Small* **2024**, *20*, 2470204.

(20) Beneventi, G. B. et al. Carbon-doped GeTe: A promising material for Phase-Change Memories. *Solid-State Electron.* **2011**, *65-66*, 197.

(21) Chahine, R.; Tomelleri, M.; Paterson, J.; Bernard, M.; Bernier, N.; Pierre, F.; Rouchon, D.; Jannaud, A.; Mocuta, C.; Giordano, V. M.; Hippert, F.; Noé, P. Nanocomposites of chalcogenide phase-change materials: from C-doping of thin films to advanced multilayers. *J. Mater. Chem. C* **2023**, *11*, 269–284.

(22) Tholapi, R.; Gallard, M.; Burle, N.; Guichet, C.; Escoubas, S.; Putero, M.; Mocuta, C.; Richard, M.-I.; Chahine, R.; Sabbione, C.; Bernard, M.; Fellouh, L.; Noé, P.; Thomas, O. Stress Buildup Upon Crystallization of GeTe Thin Films: Curvature Measurements and Modelling. *Nanomater.* **2020**, *10*, 1247.

(23) Gallard, M.; Amara, M. S.; Putero, M.; Burle, N.; Guichet, C.; Escoubas, S.; Richard, M.-I.; Mocuta, C.; Chahine, R. R.; Bernard, M.; Kowalczyk, P.; Noé, P.; Thomas, O. New insights into thermomechanical behavior of GeTe thin films during crystallization. *Acta Mater.* **2020**, *191*, 60–69.

(24) Loudon, R. Theory of Surface-Ripple Brillouin Scattering by Solids. *Phys. Rev. Lett.* **1978**, *40*, 581–583.

(25) Djemia, P.; Ganot, F.; Moch, P.; Branger, V.; Goudeau, P. Brillouin scattering investigation of elastic properties of Cu–Mo solid solution thin films. *J. Appl. Phys.* **2001**, *90*, 756–762.

(26) Djemia, P.; Ganot, F.; Dugautier, C.; Quilichini, M. Brillouin scattering from the icosahedral quasicrystal Al70.4Mn8.4Pd21.2. *Solid State Commun.* **1998**, *106*, 459–461.

(27) Auld, B. A. In *Acoustic field and waves in solids*; Wiley, Ed.; New York, 1973; Vol. 1; p 368.

(28) Walmsley, B. A.; Liu, Y.; Hu, X. Z.; Bush, M. B.; Dell, J. M.; Faraone, L. Poisson's Ratio of Low-Temperature PECVD Silicon Nitride Thin Films. *J. Microelectromechanical Syst.* **2007**, *16*, 622–627.

(29) Vila, M.; Cáceres, D.; Prieto, C. Mechanical properties of sputtered silicon nitride thin films. *J. Appl. Phys.* **2003**, *94*, 7868–7873.

(30) Hill, R. Elastic properties of reinforced solids: some theoretical principles. *J. Mech. Phys. Solids* **1963**, *11*, 357–372.

(31) Jana, R.; Savio, D.; Deringer, V. L.; Pastewka, L. Structural and elastic properties of amorphous carbon from simulated quenching at low rates. *Model. Simul. Mater. Sci. Eng.* **2019**, *27*, 085009.

(32) Kamitakahara, W. A.; Brockhouse, B. N. Vibrations of a mixed crystal: Neutron scattering from $Ni_{55}Pd_{45}$. *Phys. Rev. B* **1974**, *10*, 1200–1212.

(33) Kamitakahara, W. A.; Taylor, D. W. Comparison of single-site approximations for the lattice dynamics of mass-disordered alloys. *Phys. Rev. B* **1974**, *10*, 1190–1199.

(34) Gurunathan, R.; Hanus, R.; Dylla, M.; Katre, A.; Snyder, G. J. Analytical Models of Phonon Point-Defect Scattering. *Phys. Rev. Appl.* **2020**, *13*, 034011.

(35) Slack, G. A.; Galginaitis, S. Thermal Conductivity and Phonon Scattering by Magnetic Impurities in CdTe. *Phys. Rev.* **1964**, *133*, A253–A268.

(36) Campi, D.; Paulatto, L.; Fugallo, G.; Mauri, F.; ; Bernasconi, M. First-principles calculation of lattice thermal conductivity in crystalline phase change materials: GeTe, Sb_2Te_3, and $Ge_2Sb_2Te_5$. *Phys. Rev. B* **2017**, *95*, 024311.

(37) Ziman, J. M. *Electrons and Phonons: The Theory of Transport Phenomena in Solids*; Oxford University Press, 1960.

(38) Jiang, P.; Lindsay, L.; Huang, X.; Koh, Y. K. Interfacial phonon scattering and transmission loss in >1 µm thick silicon-on-insulator thin films. *Phys. Rev. B* **2018**, *97*, 195308.

(39) Ghosh, K.; Kusiak, A.; Noé, P.; Cyrille, M.-C.; Battaglia, J.-L. Thermal conductivity of amorphous and crystalline GeTe thin film at high temperature: Experimental and theoretical study. *Phys. Rev. B* **2020**, *101*, 214305.

TOC Graphic

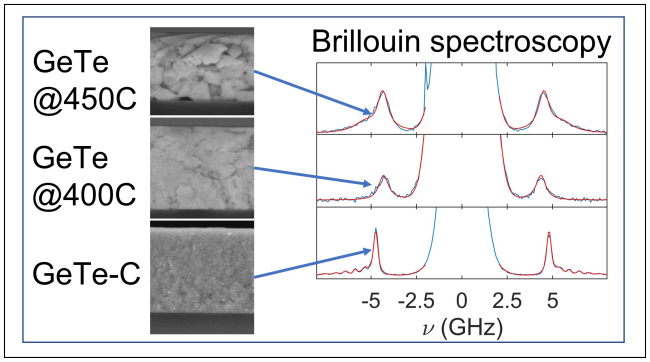
GeTe
@450C
GeTe
@400C
GeTe-C
Brillouin spectroscopy
-5 -2.5 0 2.5 5
ν (GHz)